



## Characterization of thin anodic oxides of Ti–Nb alloys by electrochemical impedance spectroscopy

Michael Teka Woldemedhin<sup>a,b</sup>, Dierk Raabe<sup>a</sup>, Achim Walter Hassel<sup>a,b,\*</sup>

<sup>a</sup> Max Planck Institut für Eisenforschung GmbH, Max Planck Str. 1, D-40237 Düsseldorf, Germany

<sup>b</sup> Institute for Chemical Technology of Inorganic Materials, Johannes Kepler University, Altenberger Str. 69, A-4040 Linz, Austria

### ARTICLE INFO

#### Article history:

Received 1 December 2011

Received in revised form 6 June 2012

Accepted 7 June 2012

Available online 18 June 2012

#### Keywords:

Anodic oxide

Electrochemical impedance spectroscopy

Mott–Schottky analysis

### ABSTRACT

Electrochemical impedance spectroscopy was used to study the interface between the anodic oxide formed on Ti–Nb alloys with specific compositions of Ti–10 wt.% Nb and Ti–20 wt.% Nb and the electrolyte. The anodic oxides were grown in an acetate buffer of pH 6.0 by using cyclic voltammetry electrochemical technique in which the potential is scanned at a rate of 100 mV s<sup>-1</sup>. The potential applied starts from 0 V and increasing at steps of 1 V till 8 V which allows to study the mechanism and the kinetics involved during the oxide growth. The electrochemical impedance measurements were started prior to applying any potential so that the electronic properties of the native oxide on the Ti–Nb alloys can be determined. The electrochemical measurements were then carried out after each oxide growth so that the electronic properties of the previously grown oxide can also be determined. The variation of the capacitance of the respective oxides determined from the impedance measurements with the applied potential enables the calculation of the relative permittivity of the respective oxides on the two alloys. Moreover the semiconducting properties of the oxides were determined by using Mott–Schottky analysis. The Mott–Schottky analysis involves electrochemical impedance measurements at fixed frequency with increasing applied bias potential so that the variation of the capacitance of the space charge region with the applied potential can be followed. The oxides from both alloys showed an n-type semiconducting property with  $7.5 \times 10^{18} \text{ cm}^{-3}$  and  $2.4 \times 10^{19} \text{ cm}^{-3}$  donor concentration for Ti–10 wt.% Nb and Ti–20 wt.% Nb alloys respectively.

© 2012 Elsevier Ltd. All rights reserved.

### 1. Introduction

Monitoring of toxic and flammable gases in both domestic and industrial environments using metal oxides as solid based semiconductor gas sensors have been of interest due to their high sensitivity to pollutant gases, small size and low cost. TiO<sub>2</sub> is the prime choice among these metal oxides for its ability to monitor both indoor and outdoor air quality [1]. This is one aspect of the potential application of TiO<sub>2</sub>.

Titanium discovered in 1791 played an important role in the daily activities of human beings since its commercial inception in the early 1950s because its light weight and corrosion resistance. From that time onwards titanium and its alloys have been used in aerospace, chemical industries, power plants, medical prostheses

[2], military [3] and sporting goods [4]. Based on their crystal structure Ti and its alloys can be classified into three groups:  $\alpha$ -, ( $\alpha + \beta$ )- and  $\beta$ -type. The  $\alpha$ -type is characterized by hexagonal close packed (hcp) crystal structure,  $\beta$ -type by body centered cubic (bcc) crystal structure and ( $\alpha + \beta$ )-type alloys are made of a mixture of the two crystal structures [5,6].

TiO<sub>2</sub> is spontaneously formed when bare titanium or its alloys come in contact with air due to the high affinity of titanium for oxygen. The native oxide formed which has a thickness of 1.3–5.4 nm [7] is responsible for the excellent corrosion resistance of titanium and its alloys by protecting the underlying material from further electrochemical activity. This is due to the low level of electronic conductivity [8], thermodynamically great stability [9] and low ion formation tendency in aqueous environments [10,11]. These properties of the TiO<sub>2</sub> layer are also the reason behind the biocompatibility of titanium implants when they are used in place of a hard tissue in the human body, since the interface between the implant material and the surrounding biological environment involves the oxide layer rather than the bulk titanium itself. TiO<sub>2</sub> has similar relative permittivity to an adsorbed water molecule,

\* Corresponding author at: Johannes Kepler University, Institute for Chemical Technology of Inorganic Materials, Altenberger Str. 69, 4040 Linz, Austria.  
Tel.: +43 732 2468 8700; fax: +43 732 2468 8905.

E-mail addresses: [hassel@elchem.de](mailto:hassel@elchem.de), [achimwalter.hassel@jku.at](mailto:achimwalter.hassel@jku.at) (A.W. Hassel).

an additional reason for the exhibited biocompatibility. Ti–6Al–4V has been widely used compared to the other titanium alloys as bio-material in restorative surgery, orthopedic implants, pace makers and heart valves [12]. Nevertheless, reports showed that there is leaching of Al and V from the alloy to the surrounding biological environment which causes an undesirable tissue response. The release of these elements can lead local discoloration, inflammatory reactions [13,14], neurological disorders such as Alzheimer [15]. This problem of cytotoxicity can be avoided by alloying titanium with other elements such as Nb, Zr, Mo and Ta in place of Al and V. The suitability of these alloys as biomaterials have been extensively investigated and reported elsewhere [16–21]. Among these alloys the Ti–Nb draw considerable attention as a biomaterial [2]. Moreover, some of the Ti–Nb alloys exhibit shape memory effect. The shape memory effect was first reported by Baker [22] for Ti–Nb alloys with a composition of Ti–35 wt.% Nb. The shape memory effect was also noticed in Ti–(20–27) at.% Nb [23], Ti–Nb based ternary alloys such as Ti–Nb–Al [24], Ti–Nb–O [25], Ti–Nb–Ta [26,27], Ti–Nb–Zr [28] and quaternary alloys such as Ti–Nb–Zr–Ta [29]. The observed shape memory effect in Ti–Nb based alloys is attributed to a reversible transformation between martensitic  $\alpha''$  and austenitic  $\beta$  phases [30].

It is well known also that anodic oxides of valve metals like Ti and Nb show current rectification in metal/metal oxide/electrolyte system. Because of the high relative permittivity values, the oxides of these metals have important applications in electrolytic capacitors [31], DRAM storage capacitors and MOSFET gate oxides [32]. Other materials such as dielectric ceramics and ferroelectric materials have even much higher relative permittivity values up to 100,000 [33]. However, the incorporation of these materials as thin films into electronic devices has been difficult unlike the ultra thin anodic oxides of Ti, Nb and other valve metals to get a compromise between the capacitance and volume of the capacitor. Small defect concentration, capacitance independent of bias potential and small leakage current are the some of the prerequisites that need to be fulfilled for the oxides of Ti and Nb to be used at an industrial scale for the production of capacitors [32].

Despite their potential application, only a few papers addressed the passivity and electronic properties of the anodic oxides on Ti–Nb alloys. Semboshi et al. studied the structural and dielectric properties of anodic oxides on Ti–Nb alloys with Ti contents in the alloy ranging from 0 to 15 at.%. It was reported that the oxide films contained amorphous and partly crystalline titanium and niobium oxides. The increase of Ti content in the alloy leads to an increase in the amount of the titanium oxide in the mixed oxide. The growing content of titanium oxide in the mixed oxide increased the capacitance of the mixed oxide film due to the higher dielectric number of titanium oxide up to a composition of 3 at.% Ti in the substrate alloy [34]. Mardare et al. [35] reported the high-throughput growth and characterization of anodic oxides on the surface of Ti–Nb thin film libraries where issues like the passivity and electronic properties of the anodic oxides were discussed for the largest spread of alloys reported so far.

Passivity and characterization of the anodic oxides of a  $\beta$ -type Ti–Nb alloy with a specific composition of Ti–30 at.% Nb were also investigated by electrochemical impedance spectroscopy and reported earlier [36,39]. The issues of the passivity and oxide characterization of this alloy were also done using a scanning droplet cell on the single grains [37] and grain boundaries [38,39] in relation to the crystallographic orientation of the grains determined by electron backscatter diffraction (EBSD).

In this paper, the issues of passivity and oxide characterization by electrochemical impedance spectroscopy were extended to two ( $\alpha + \beta$ )-type Ti–Nb alloys with compositions Ti–10 wt.% Nb and Ti–20 wt.% Nb. These two alloys are ( $\alpha + \beta$ )-type titanium alloys as shown in the phase diagram for Ti–Nb system.

## 2. Experimental

### 2.1. Sample surface preparation

The Ti–Nb alloys of 1 cm<sup>2</sup> in area are successively ground with silicon carbide grinding papers starting from the coarse abrasive of 220 grit and progressing to the finer abrasives of 2500 and 4000 in the presence of running water. The sample surfaces were then polished with a silica suspension on a nylon cloth disc to remove the damage from the grinding process and thereby getting a smooth surface with less deformation to the crystal structure of the sample surface. One fraction by volume of 30% H<sub>2</sub>O<sub>2</sub> is added to five parts of the silica suspension for polishing the Ti–Nb alloys for better results. The last seconds of the polishing procedure were carried out in the presence of running water to clean the sample surface from silica residuals. The true microstructure of the sample surface is revealed by electropolishing the sample surface potentiostatically at 8 V in a 3 M methanolic sulfuric acid solution kept at –22 °C [40]. The sample surface is cleaned in an ultrasonic bath of ethanol and water, rinsed with ethanol and dried with compressed nitrogen gas to remove leftovers from the sample surface preparation.

### 2.2. Electron backscatter diffraction (EBSD)

To get an insight into the microstructure of the Ti–Nb alloys and thereby confirming that the sample surface is free of deformation EBSD scans were carried out on the two alloys.

Field emission scanning electron microscope (Zeiss 150XB) equipped with an EBSD unit was used for the EBSD measurements with an acceleration voltage of 20 kV and step size of 150 nm on a sample surface tilted 70° from the horizontal for orientation mapping.

### 2.3. Electrochemical measurements

Cyclic voltammetry is the electrochemical technique used to grow the oxides so that the mechanism of the oxide growth and the kinetics involved during oxide growth can be followed. The applied potential starting from 0 V and increasing in steps of 1 V to 8 V was scanned at a rate of 100 mV s<sup>-1</sup> on a sample immersed in an acetate buffer of pH 6.0. Electrochemical impedance measurements were carried out before applying potential in a frequency range of 50 kHz to 10 mHz with an AC perturbation voltage of 10 mV to study the oxide/electrolyte interface of the native oxide formed from air passivation of the Ti–Nb alloys. Successive electrochemical impedance measurements were carried out right after each potential sweep by cyclic voltammetry to study the interface between the previously formed oxide and the electrolyte. For determining the semiconducting properties of the oxides, Mott–Schottky analysis was done on an oxide grown potentiostatically at 3 V for 1000 s. An Impedance/Gain phase analyzer (Solartron SI 1260) coupled with a PAR Potentiostat/Galvanostat Model 283 (Princeton Applied Research) was used for the electrochemical measurements. All the potentials mentioned in this paper refer to the standard hydrogen electrode (SHE) potential.

### 2.4. Electrochemical cell

A double glass walled cell with seven outlets, which are used to connect the gas inlet/outlet, counter, reference and working electrodes was used for the electrochemical measurements. A commercial Ag/AgCl/3 M KCl (Metrohm) and a gold plate of 2 cm<sup>2</sup> area were used respectively as reference and counter electrodes. All the experiments were carried out at room temperature and the

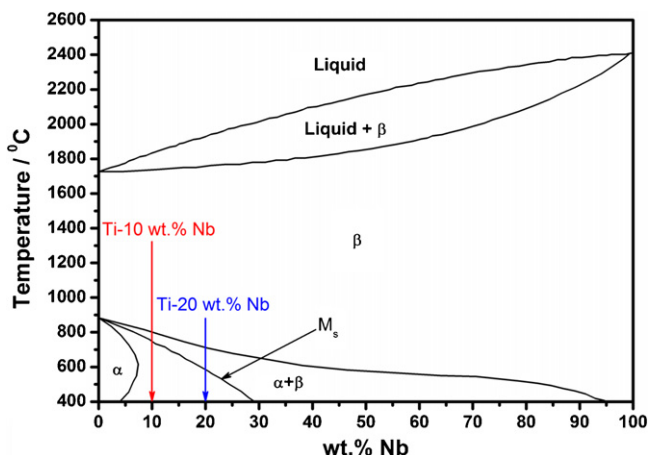


Fig. 1. Phase diagram of the Ti–Nb system [2].

electrolyte solution was purged with nitrogen gas prior to starting the experiments to drive the dissolved oxygen out (Fig. 1).

### 3. Results and discussion

#### 3.1. Microstructure of Ti–10 wt.% Nb and Ti–20 wt.% Nb alloys

Fig. 2 shows the optical micrograph of the boundary between the oxidized which has a golden color and the unoxidized surface of the two Ti–Nb alloys. From the picture it is clear that the two alloys are made of large grains. But inside these large grains there are subgrains with sizes in the order of 10  $\mu\text{m}$  made up of the hexagonal and body centered cubic crystal structures as it is revealed from

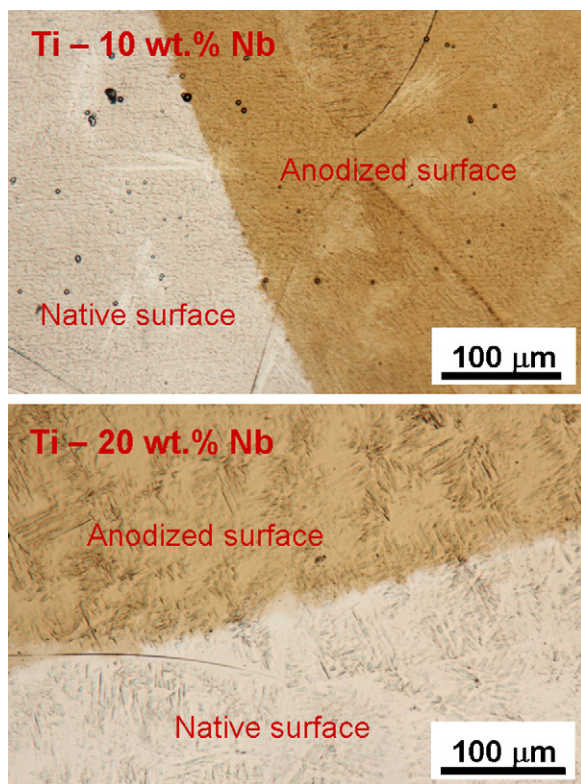


Fig. 2. Optical micrograph of the boundary between the oxidized (golden color) and the unoxidized surface of Ti–10 wt.% Nb and Ti–20 wt.% Nb sample. (For interpretation of the references to color in this figure legend, the reader is referred to the web version of the article.)

the EBSD measurements. Inverse pole figure and the corresponding image quality which gives information about the contrast between the bands is shown in Fig. 3

#### 3.2. Cyclic voltammetry

The successive cyclic voltammograms recorded during oxide growth for the two Ti–Nb alloys is shown in Fig. 4. A sharp overshoot in current density is observed in the first cycle for the two alloys which broadens and later disappears after the second cycle onwards. The observed overshoot results from the complete overlap of oppositely charged ion clouds of metal ions of the substrate alloys and oxide anions during field assisted migration of the ions to the oxide/electrolyte and metal/oxide interfaces respectively as explained by the extended high field model [41]. The formation of this space charge region during the overlap of the ions leads to a retardation in the migration and arrival of the ions at the two interfaces where the new oxide is formed. Thus the overshoot is a sign of the delay in the kinetics of the oxide formation. In the intermediate potential regions the overshoot is no more observed, rather a current plateau is observed until the upper oxide formation potential. The current plateau indicates the absence of any side electron transfer reactions which would result in oxygen evolution and the sole reaction involved is an ion transfer reaction resulting in the constant thickening of the oxide according to the high field mechanism [41]. During the reverse cathodic sweep after reaching the upper oxide formation, the current falls rapidly towards zero. In the subsequent anodic sweep the current stays to the minimum until it surpasses the oxide formation potential of the previously grown oxide due to the current rectification of the oxides. As the applied potential is increased the migration of the oppositely charged ions towards the two interfaces dominates the kinetics of the oxide formation resulting in delayed oxide formation evident from the smeared out increase in the current density as shown towards the last cycles of the cyclic voltammograms of Fig. 4. The retardation in the kinetics of the oxide formation can also be observed from the increasing gap between the cathodic curve and the anodic curve of the subsequent cycle.

The area under each cycle in the cyclic voltammogram is proportional to the charge density consumed to grow the respective oxides. The charge density can then be related to the thickness of the oxide as:

$$d = \frac{MQ}{zrF\rho} \quad (1)$$

where  $d$  is the oxide thickness,  $M$  is molecular weight,  $Q$  is the charge density,  $z$  is number of exchanged electrons per formula unit,  $r$  is roughness factor which was assumed to be equal to one for an electropolished surface and  $\rho$  is density of the mixed oxide [42]. The density of the mixed oxide of titanium and niobium is determined based on the compositions of the constituent elements of the substrate alloys where a value of 4.22 and 4.36  $\text{g cm}^{-3}$  were taken for pure  $\text{TiO}_2$  and  $\text{Nb}_2\text{O}_5$  respectively.

The thickness of the oxide  $d$  is related to the applied potential  $E$  as:

$$d = k(E - E_{\text{ox}}) \quad (2)$$

where  $k$  is the formation factor given in  $\text{nm V}^{-1}$  and  $E_{\text{ox}}$  is the equilibrium potential of the oxide electrode [42,7]. A plot of the charge ( $Q$ ) consumed to grow the oxides versus the formation potential is presented in Fig. 5. A linear correlation is observed between the charge density and the applied potential for both of the Ti–Nb alloys. This implies the process was Faradaic and exclusive ionic conductivity disables the electron transfer on the electrode. The oxide formation factor ( $k$ ) can thus be calculated from the slope of the linear fit of such plot based on Eqs. (1) and (2). A value of 2.45

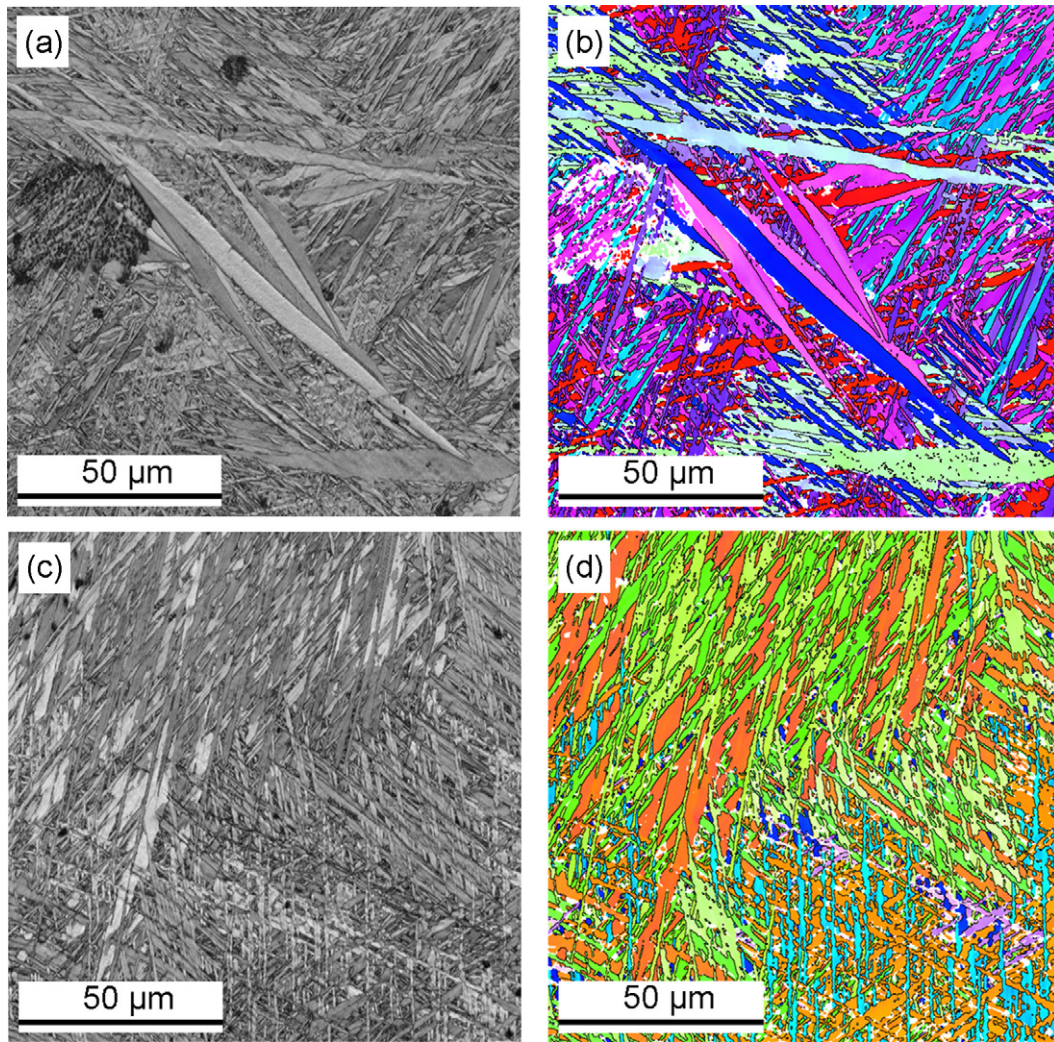


**Fig. 3.** Image quality map of (a) Ti–10 wt.% Nb and (c) Ti–20 wt.% Nb; inverse pole figure of (b) Ti–10 wt.% Nb and (d) Ti–20 wt.% Nb.

and  $2.49 \text{ nm V}^{-1}$  was calculated from the slope for the Ti–10 wt.% Nb and Ti–20 wt.% Nb alloys respectively.

### 3.3. Electrochemical impedance spectroscopy

Bode plot representation of the impedance spectra for the oxides on the two Ti–Nb alloys, Ti–10 wt.% Nb and Ti–20 wt.% Nb are shown

in Figs. 6 and 7 respectively. At high frequencies ( $>10 \text{ kHz}$ ) a constant value of impedance  $18 \pm 1.1 \Omega \text{ cm}^2$  and the phase shift close to zero indicates a pure resistive behavior which is a sole contribution from the electrolyte resistance. As the frequency is decreasing and reaching the intermediate frequency range, the impedance increases with the applied potential proving that the oxide is thickening with the applied potential for both of the alloys. The phase

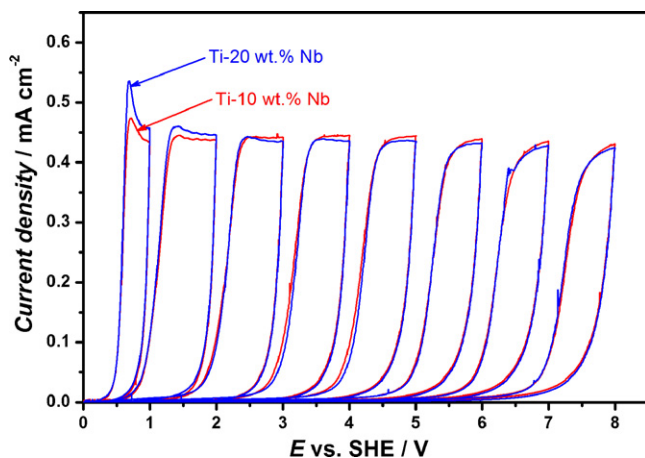


**Fig. 4.** Cyclic voltammograms from anodization of Ti–10 wt.% Nb and Ti–20 wt.% Nb.

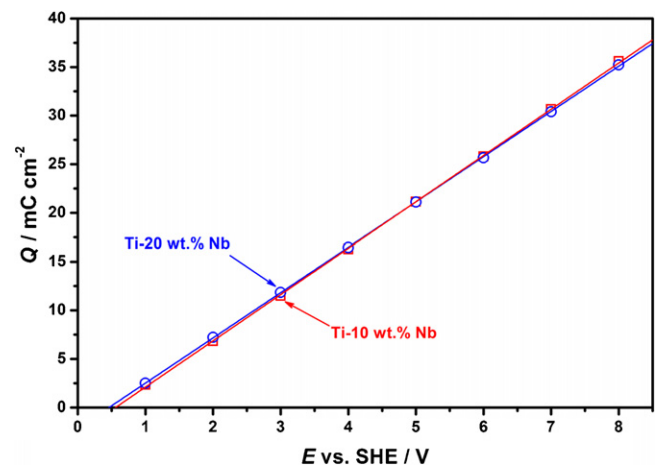


**Fig. 5.** Plot of the charge density versus the potential applied to grow the oxides.

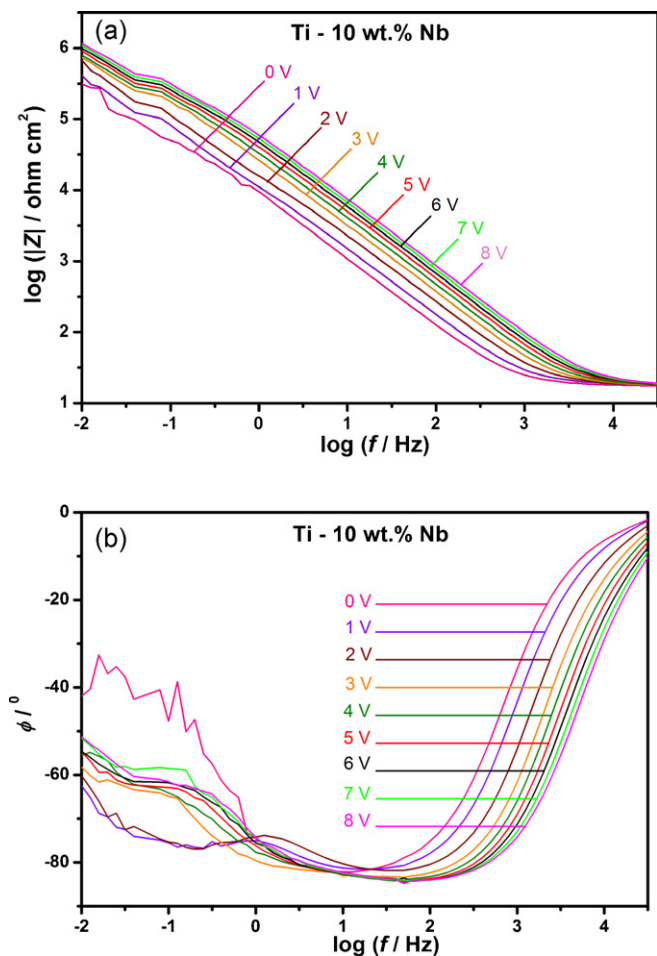


Fig. 6. (a and b) Bode plot representation of the EIS spectra for the anodic oxides of Ti-10 wt.% Nb.

shift recorded from the native oxide prior to any potential application showed one time constant with the value around  $80^\circ$  indicating a near capacitive behavior for both of the Ti-Nb alloys. However the phase shift recorded after the application of potential on the two alloys is different. A clear two time constant is observed from the impedance spectra on the Ti-10 wt.% Nb alloy especially after an oxide growth with 1 V and 2 V. Fig. 8 shows the equivalent circuit proposed to fit the impedance spectra of Ti-10 wt.% Nb alloy which contains a series connection of two resistor-capacitor (RC), connected in parallel, with the electrolyte resistance  $R_s$  indicating that there are two distinct layers of oxides with different electrical properties. However the phase shift recorded from the Ti-20 wt.% Nb alloy showed only one time constant for all of the nine impedance spectra. The phase shift reached a value around  $-86^\circ$  indicating a near capacitive behavior of the oxides from this alloy. The equivalent circuit used to fit the impedance spectra from the Ti-20 wt.% Nb alloy is shown in Fig. 8. A constant phase element is used to fit the impedance spectra as shown in the equivalent circuits proposed for the oxides on the two alloys. The impedance of a constant phase element is given by:

$$Z(\omega) = \frac{1}{Q} (i\omega)^{-n} \quad (3)$$

where  $i$  is a complex number,  $Q$  constant and  $-1 \leq n \leq 1$ . The value of  $n$  tells whether the constant phase element acts like an inductor, resistor or capacitor. When  $n = -1$  the constant phase element acts as an inductor,  $n = 0$  as pure resistor and  $n = 1$  as an ideal capacitor [43]. The value of  $n$  is in the range of 0.90–0.93 and 0.94–0.97 for the

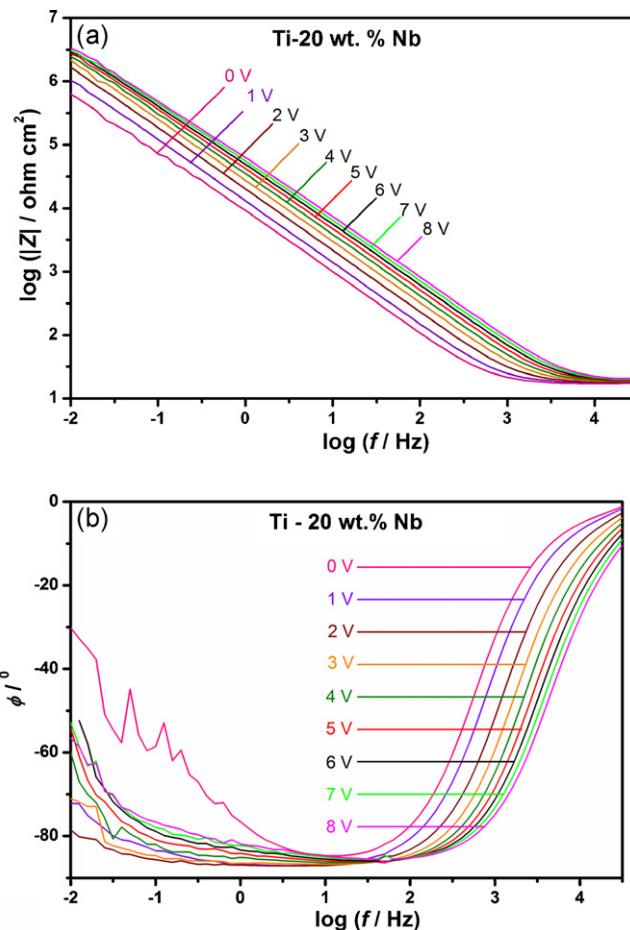


Fig. 7. (a and b) Bode plot representation of the EIS spectra for the anodic oxides of Ti-20 wt.% Nb.

constant phase elements used in the equivalent circuits proposed for Ti-10 wt.% Nb and Ti-20 wt.% Nb alloys respectively as shown in Tables 1 and 2. These values indicate how much the oxides of the two alloys especially the oxides of Ti-20 wt.% Nb alloy are close to being an ideal capacitor. The experimental and the fitted curves for

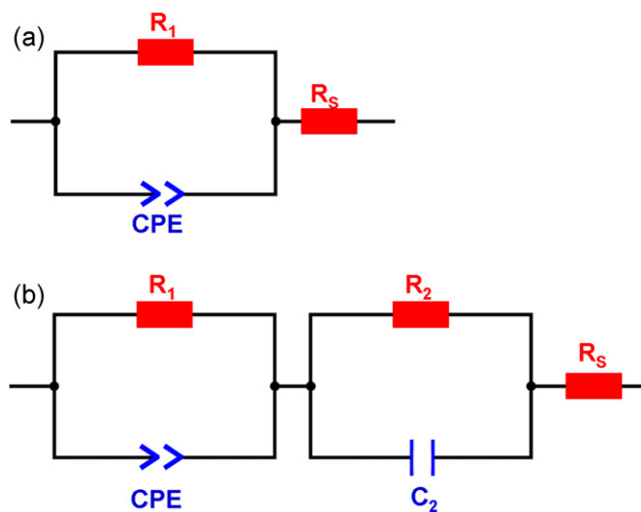


Fig. 8. Equivalent circuits used to fit the impedance spectra: (a) for the native oxide of Ti-10 wt.% Nb and the oxides of Ti-20 wt.% Nb and (b) for the anodic oxides of Ti-10 wt.% Nb after application of potential.

**Table 1**

The values of the circuit elements from the proposed equivalent circuit of the oxide on Ti–10 wt.% Nb alloy.

$E$ (V)	$R_1$ ( $M\Omega\text{ cm}^2$ )	$CPE_1$ ( $\mu\Omega^{-1}\text{ s}^n\text{ cm}^{-2}$ )	$n$	$R_2$ ( $k\Omega\text{ cm}^2$ )	$C_1$ ( $\mu\text{F cm}^{-2}$ )	$R_s$ ( $\Omega\text{ cm}^2$ )
0	0.07	19.83	0.93	–	–	17.83
1	1.20	18.73	0.91	2.06	55.14	18.55
2	1.71	12.83	0.92	2.63	27.56	18.46
3	2.01	10.49	0.91	51.87	16.88	18.13
4	1.94	8.98	0.91	54.06	11.45	18.25
5	2.13	7.87	0.91	58.99	8.34	18.57
6	2.32	7.09	0.91	68.30	6.65	18.56
7	2.28	6.47	0.90	81.03	5.64	18.55
8	2.35	5.69	0.90	75.58	5.12	18.57

some of the impedance spectra from the two alloys Ti–10 wt.% Nb and Ti–20 wt.% Nb is shown in Figs. 9 and 10 respectively.

One of the important attributes of the oxides of valve metals is their high dielectric number for potential applications in the electronic industry. The dielectric number of these oxides can be determined from the impedance in the intermediate frequency range. The impedance in this region is almost a sole contribution of the capacitive reactance of the oxides which is related to capacitance as:

$$\chi_C = \frac{1}{2\pi f C} \quad (4)$$

where  $\chi_C$  is the capacitive reactance,  $f$  frequency where the phase shift reaches the maximum value and  $C$  capacitance [44]. The capacitance of the oxide  $C_{ox}$  is calculated from the total electrode capacitance  $C$  by taking into consideration the capacitance of the Helmholtz double layer  $C_H$ . Since the two capacitances are in parallel the equivalent capacitance is written as:

$$\frac{1}{C} = \frac{1}{C_{ox}} + \frac{1}{C_H} \quad (5)$$

A value of  $20\ \mu\text{F cm}^{-2}$  [45,46] commonly used in the literature for the Helmholtz layer capacitance is taken to calculate the oxide capacitance. The capacitance  $C_{ox}$  is related to the oxide thickness  $d$  using the equation for a parallel plate condenser as:

$$C_{ox} = \frac{\epsilon_r \epsilon_0}{d} \quad (6)$$

where  $\epsilon_r$  is the dielectric number of the oxide and  $\epsilon_0$  is the permittivity of vacuum. Inserting Eq. (2) in Eq. (6) and rearranging yields:

$$\frac{1}{C_{ox}} = \frac{k}{\epsilon_r \epsilon_0} (E - E_{ox}) \quad (7)$$

Thus the slope from the plot of the  $C_{ox}^{-1}$  versus the applied potential  $E$  will give the relative permittivity values of the respective oxides based on the value of the formation factor  $k$  determined earlier from the cyclic voltammetry measurements. A value of 48 and 50.5 were determined for the relative permittivity value of the mixed oxides of Ti–10 wt.% Nb and Ti–20 wt.% Nb respectively as shown in Fig. 11.

**Table 2**

The values of the circuit elements from the proposed equivalent circuit of the oxide on Ti–20 wt.% Nb alloy.

$E$ (V)	$R_1$ ( $M\Omega\text{ cm}^2$ )	$CPE_1$ ( $\mu\Omega^{-1}\text{ s}^n\text{ cm}^{-2}$ )	$n$	$R_s$ ( $\Omega\text{ cm}^2$ )
0	0.09	18.18	0.97	16.90
1	3.28	12.98	0.97	17.41
2	9.91	8.47	0.97	17.57
3	6.93	6.21	0.96	17.82
4	5.77	4.96	0.96	17.81
5	5.29	3.71	0.95	18.79
6	5.05	3.66	0.95	18.55
7	5.39	3.32	0.94	17.71
8	6.09	2.98	0.94	17.67

The value of the circuit elements from the equivalent circuits proposed for the two Ti–Nb alloys Ti–10 wt.% Nb and Ti–20 wt.% Nb are tabulated in Tables 1 and 2 respectively. The equivalent circuit proposed for Ti–10 wt.% Nb is in the literature for having a bilayer structure for the oxide consisting of a barrier and porous layers for different kind of electrolytes used especially for experiments where the oxide growth takes place in an aggressive electrolyte. However this work is done in an acetate buffer where the formation of a porous type oxide structure is less likely. The observed two time constants however can be explained by taking into consideration the formation of suboxides of the constituent elements of the alloy. Titanium and niobium are transition elements which can form different oxides and suboxides with different physical properties due the variable valencies they exhibit. Among these suboxides

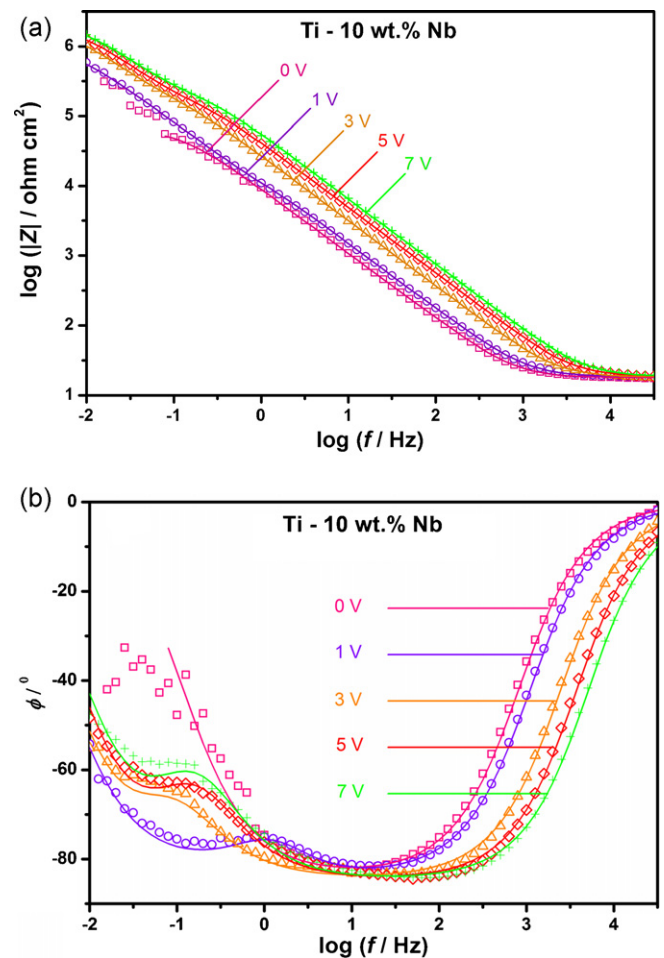


**Fig. 9.** (a and b) Bode plot representation for some of the experimental and fitted curves of the EIS spectra for the anodic oxides of Ti–10 wt.% Nb. Symbols represent the experimental data solid lines fitted curves.

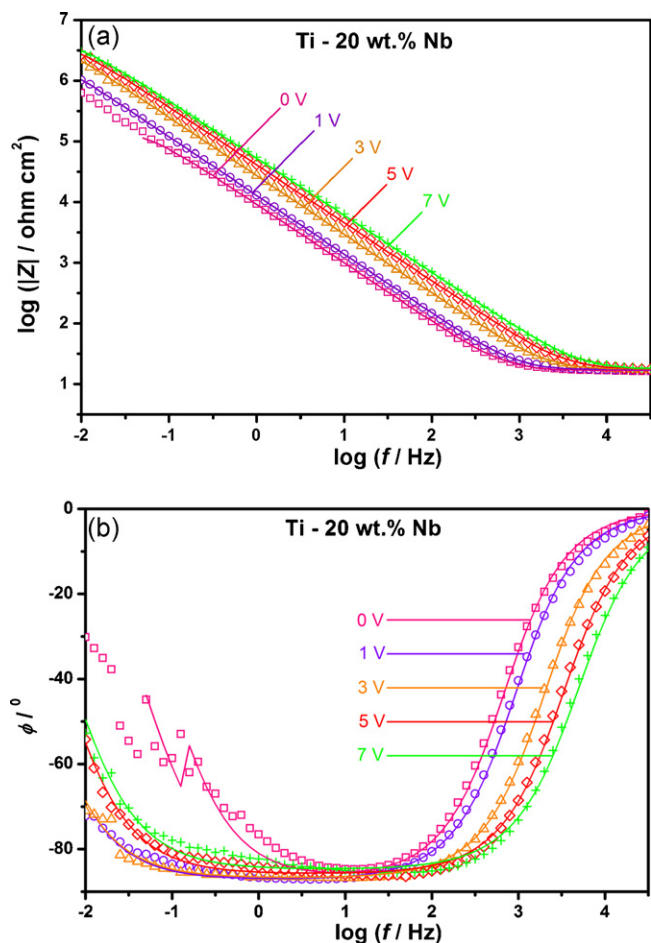


Fig. 10. (a and b) Bode plot representation for some of the experimental and fitted curves of the EIS spectra for the anodic oxides of Ti-20 wt.% Nb. Symbols represent the experimental data solid lines fitted curves.

niobium monoxide NbO is a conductor [47,48]. The formation of NbO will increase the electrical conductivity of the whole oxide which is exhibited by  $R_2$  value of 2.06 and 2.63  $k\Omega\text{cm}^2$  for the oxides grown at 1V and 2V respectively as shown in Table 1 for Ti-10 wt.% Nb alloy. The value of the  $R_2$  increases drastically from 2.63  $k\Omega\text{cm}^2$  to 51.87  $k\Omega\text{cm}^2$  up on moving from the oxide grown at 2V to 3V. The oxidation of the NbO to higher oxidation states to form Nb<sub>2</sub>O<sub>5</sub> results in decreasing the conductivity and

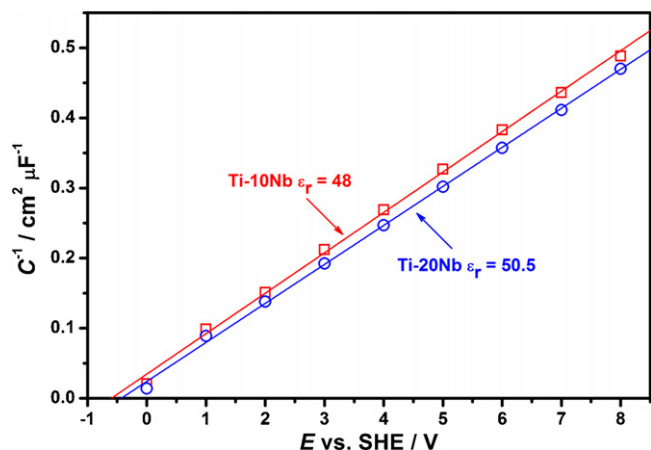


Fig. 11. Plot of the inverse capacitance of the anodic oxides versus the potential applied to grow the oxides.

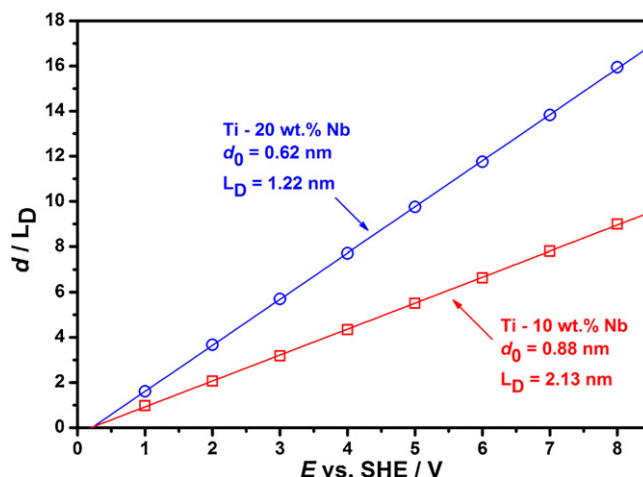


Fig. 12. Plot of the ratio of the oxide thickness ( $d$ ) and Debye length ( $L_D$ ) versus the potential applied to grow the oxides.

thereby increasing the resistance as shown in the value of  $R_2$ . Similar observations were reported by Milosev et al. [49] from the characterization of the passive film formed on a Ti-6Al-7Nb  $\alpha + \beta$ -type Ti alloy by electrochemical impedance spectroscopy and XPS measurements. The presence of suboxides of niobium were confirmed by XPS measurements and the value of the resistance increased drastically for potentials  $\geq 3\text{V}$  similar to the change in  $R_2$  observed for this alloy as well.

Another important parameter in the study of oxide growth and characterization is the determination of the native oxide thickness  $d_0$ . The thickness of the native oxide on both alloys prior to any potential application is determined from the first impedance spectra using Eq. (6) based on the respective value of the relative permittivity of the two mixed oxides. The native oxide thickness is determined to be 0.88 and 0.62 nm respectively for Ti-10 wt.% Nb and Ti-20 wt.% Nb alloys. From this initial thickness the oxide thickness on both alloys continue to grow with the applied potential as shown in Fig. 12. Fig. 12 shows the plot of the ratio between the oxide thickness and the Debye length  $L_D$  with the applied potential. The Debye length is given by:

$$L_D = \frac{1}{e} \left( \frac{\epsilon_r \epsilon_0 k T}{2 N_D} \right)^{1/2} \quad (8)$$

where  $e$  is the electronic charge,  $k$  Boltzmann constant,  $T$  absolute temperature and  $N_D$  is the donor concentration [50]. The value of the donor concentration  $N_D$  for the respective oxides is taken from the Mott-Schottky analysis carried out on the two alloys as explained in detail in the next section. Thus a Debye length of 2.13 and 1.22 nm were calculated for the oxides of Ti-10 wt.% Nb and Ti-20 wt.% Nb respectively. The Debye length of the oxide of Ti-10 wt.% Nb is almost twice that of the Ti-20 wt.% Nb alloy.

#### 3.4. Mott-Schottky analysis

Mott-Schottky analysis was employed to study the semiconducting properties of the mixed anodic oxides grown on Ti-10 wt.% Nb and Ti-20 wt.% Nb alloys. It gives qualitative as to the type of the semiconductor and quantitative information such as the donor concentration and flat band potentials for the mixed oxide based on the Mott-Schottky equation:

$$C_{sc}^{-2} = \left( \frac{2}{e \epsilon_r \epsilon_0 N_D} \right) \left( E - E_{fb} - \frac{kT}{e} \right) \quad (9)$$

where  $E_{fb}$  is flat band potential [51]. The analysis was carried out on an oxide potentiostatically grown at 3V for 1000 s on both alloys.

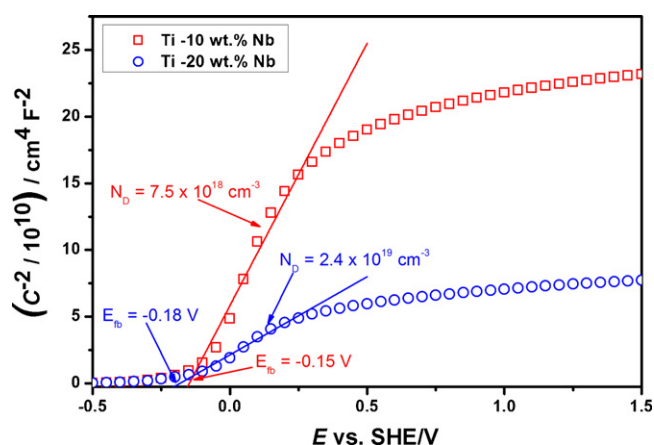


Fig. 13. Mott–Schottky plots of the oxides of Ti–10 wt.% Nb and Ti–20 wt.% Nb.

Electrochemical impedance measurements were carried out after the oxide growth at fixed frequency by sweeping the bias from 1.5 V to  $-0.5$  V in steps of 50 mV. The variation of the capacitance of the space charge region versus the applied bias potential for the mixed oxides of titanium and niobium on the two alloys is shown in the Mott–Schottky plot of Fig. 13. A linear region, 0.25 V to  $-0.25$  V, with a positive slope for the two alloys indicates an n-type semiconducting property. The donor concentration and the flat band potential of the respective oxides is calculated from the slope and intercept of the line fitted for this linear region with the potential axis as shown in Fig. 13. From the Mott–Schottky analysis a donor concentration of  $7.5 \times 10^{18} \text{ cm}^{-3}$  and  $2.4 \times 10^{19} \text{ cm}^{-3}$  were determined for Ti–10 wt.% Nb and Ti–20 wt.% Nb alloy respectively based on the relative permittivity values of the respective oxides determined in the earlier section. Likewise the flat band potentials were  $-0.15$  V and  $-0.18$  V respectively for Ti–10 wt.% Nb and Ti–20 wt.% Nb alloys. The oxide of Ti–20 wt.% Nb alloy has a donor concentration around three orders of magnitude higher than that of Ti–10 wt.% Nb alloy whereas the flat band potential is almost equivalent.

#### 4. Conclusions

The thin anodic oxides grown on the Ti–Nb alloys showed current rectification where the passage of current in both directions typical of the oxides on valve metals like Ti and Nb is impossible. The oxides on the two alloys grow according to the high field mechanism as it is evident from the current plateaus of the cyclic voltammograms shown in Fig. 4. The growth of the oxides at the initial stages showed an overshoot in current due to the delay in the oxide formation as explained by the extended high field mechanism. The observed overshoot later disappears and changed to a current plateau indicating the absence of oxygen evolution reaction unlike the conventional Ti with a hexagonal close packed lattice structure. The formation factor which is the reciprocal of the critical field strength of a certain oxide determined from the charge consumed to grow the oxides is an important parameter in the study of oxide films. The mixed oxides from the two alloys have higher relative permittivity values calculated from the plot of the inverse capacitance of the oxide with the applied potential. A linear relationship between the inverse capacitance of the oxide with the applied potential proves that the anodic oxide of the two alloys acts as dielectric material. Moreover the semiconducting properties of the oxides are assessed using Mott–Schottky analysis where both of the anodic oxides of the two alloys showed an n-type semiconducting property with different donor concentrations and an equivalent flat band potential values.

#### Acknowledgement

M.T. Woldemedhin would like to thank the International Max Planck Research School for Surface and Interface Engineering (IMPRS–SurMat) for the doctoral fellowship.

#### References

- [1] T. Anukunprasert, C. Saiwan, E. Traversa, Science and Technology of Advanced Materials 6 (2005) 359.
- [2] A. Cremasco, W.R. Osorio, C.M.A. Freire, A. Garcia, R. Caram, Electrochimica Acta 53 (2005) 4867.
- [3] E. Eisenbarth, D. Velten, M. Muller, R. Thull, J. Breme, Biomaterials 25 (2004) 5705.
- [4] C.R.M. Afonso, G.T. Alexio, A.J. Ramirez, R. Caram, Materials Science and Engineering C 27 (2007) 908.
- [5] B. Sander, D. Raabe, Materials Science and Engineering A 479 (2008) 236.
- [6] D. Raabe, B. Sander, M. Friak, D. Ma, J. Neugebauer, Acta Materialia 55 (2007) 4475.
- [7] J.W. Schultze, M.M. Lohrengel, Electrochimica Acta 45 (2000) 2499.
- [8] H. Zwitter, H.J. Plenk, Journal of Biomedical Materials Research 21 (1987) 881.
- [9] D.F. Williams, Annual Review of Materials Science 6 (1979) 237.
- [10] R.J. Solar, S.R. Pollack, E. Korostoff, Journal of Biomedical Materials Research 13 (1979) 217.
- [11] Y.T. Sul, C.B. Johansson, Y. Jeong, T. Albrektsson, Medical Engineering & Physics 23 (2001) 329.
- [12] A. Robin, O.A.S. Carvalho, S.G. Schneider, S. Schneider, Materials and Corrosion 59 (2008) 929.
- [13] J. Black, H. Sherk, J. Bonini, W.R. Rostoker, J.O. Galante, Journal of Bone and Joint Surgery A72 (1990) 126.
- [14] H.C. Amstutz, P. Campbell, N. Kossovsky, I.C. Clarke, Clinical Orthopaedics 7 (1991) 276.
- [15] T.A.G. Donato, L.H. de Almeida, R.A. Nogueira, T.C. Niemeyer, C.R. Grandini, R. Caram, S.G. Schneider, A.R. Santos Jr., Materials Science and Engineering C 29 (2009) 1365.
- [16] D. Kuroda, M. Niinomi, M. Morinaga, Y. Kato, T. Yashiro, Materials Science and Engineering A 243 (1998) 244.
- [17] M. Niinomi, D. Kuroda, K. Fukunaga, M. Morinaga, Y. Kato, T. Yashiro, A. Suzuki, Materials Science and Engineering A 263 (1999) 190.
- [18] M. Niinomi, Science and Technology of Advanced Materials 4 (2003) 445.
- [19] Y. Okazaki, E. Gotoh, Biomaterials 26 (2005) 11.
- [20] M. Ikeda, S. Komatsu, Y. Nakamura, Materials Transactions 45 (2004) 1106.
- [21] S. Miyazaki, H.Y. Kim, H. Hosoda, Materials Science and Engineering A 438 (2006) 18.
- [22] C. Baker, Metal Science Journal 5 (1971) 92.
- [23] H.Y. Kim, Y. Ikehara, J.I. Kim, H. Hosoda, S. Miyazaki, Acta Materialia 54 (2006) 2419.
- [24] Y. Fukui, T. Inamura, H. Hosoda, K. Wakashima, S. Miyazaki, Materials Transactions 45 (2004) 1077.
- [25] J.I. Kim, H.Y. Kim, H. Hosoda, S. Miyazaki, Materials Transactions 46 (2005) 852.
- [26] H.Y. Kim, T. Sasaki, K. Okutsu, J.I. Kim, T. Inamura, H. Hosoda, S. Miyazaki, Acta Materialia 54 (2006) 423.
- [27] H.Y. Kim, S. Hashimoto, J.I. Kim, T. Inamura, H. Hosoda, S. Miyazaki, Materials Science and Engineering A 417 (2006) 120.
- [28] J.I. Kim, H.Y. Kim, T. Inamura, H. Hosoda, S. Miyazaki, Materials Science and Engineering A 403 (2005) 334.
- [29] N. Sakaguchi, M. Niinomi, T. Akahori, J. Takeda, H. Toda, Materials Science and Engineering C 25 (2005) 363.
- [30] D.H. Ping, C.Y. Cui, F.X. Yin, T. Yamabe-Mitarai, Scripta Materialia 54 (2006) 1305.
- [31] D.A. Mclean, F.S. Power, Proceedings of the Institute of Radio Engineers 44 (1956) 872.
- [32] M. Schneider, S. Schroth, J. Schilm, A. Michaelis, Electrochimica Acta 54 (2009) 2663.
- [33] S. Schroth, M. Schneider, T. Mayer-Uhma, A. Michaelis, V. Klemm, Surface and Interface Analysis 40 (2008) 850.
- [34] S. Semboshi, K. Bando, N. Ohtsu, Y. Shim, T.J. Konno, Thin Solid Films 516 (2008) 8613.
- [35] A.I. Mardare, A. Savan, A. Ludwig, A.D. Wieck, A.W. Hassel, Electrochimica Acta 54 (2009) 5973.
- [36] M.T. Woldemedhin, D. Raabe, A.W. Hassel, Physica Status Solidi A207 (2010) 812.
- [37] M.T. Woldemedhin, D. Raabe, A.W. Hassel, Electrochimica Acta, submitted for publication.
- [38] M.T. Woldemedhin, D. Raabe, A.W. Hassel, Physica Status Solidi A208 (2011) 1246.
- [39] M.T. Woldemedhin, D. Raabe, A.W. Hassel, Surface reactivity of  $\beta$ -type Ti–Nb alloy, Book series, submitted for publication.
- [40] K. Fushimi, M. Stratmann, A.W. Hassel, Electrochimica Acta 52 (2006) 1290.
- [41] M.M. Lohrengel, Materials Science and Engineering R11 (1993) 243.
- [42] J.W. Schultze, A.W. Hassel, Passivity of metals, alloys and semiconductors, in: A.J. Bard, M. Stratmann (Eds.), Encyclopaedia of Electrochemistry, in: M. Stratmann, G.S. Frankel (Eds.), Corrosion and Oxide Films, vol. 4, Wiley-VCH, Weinheim, Germany, 2003, pp. 216–270, pp. 188–189.

- [43] J.R. Macdonald, *Impedance Spectroscopy: Emphasizing Solid Materials & Systems*, John Wiley & Sons, Inc., New York, 1987.
- [44] D. Kong, S. Chen, C. Wang, W. Yang, *Corrosion Science* 45 (2003) 747.
- [45] O. Kerrec, D. Devilliers, H. Groult, M. Chemla, *Electrochimica Acta* 40 (1995) 719.
- [46] V.A. Macagno, J.W. Schultze, *Journal of Electroanalytical Chemistry* 180 (1984) 157.
- [47] Y. Zhao, Z. Zhang, Y. Lin, *Journal of Physics D: Applied Physics* 37 (2004) 3392.
- [48] V.D. Jovic, B.M. Jovic, *Journal of the Serbian Chemical Society* 73 (2008) 351.
- [49] I. Milosev, T. Kosec, H.H. Strehblow, *Electrochimica Acta* 53 (2008) 3547.
- [50] R. Memming, *Semiconductor Electrochemistry*, Wiley-VCH, Weinheim, 2000.
- [51] R. Silva, M.A. Barbosa, B. Rondot, M.C. Belo, *British Corrosion Journal* 25 (1990) 136.